

See discussions, stats, and author profiles for this publication at: <https://www.researchgate.net/publication/296474014>

# On the modeling of hyperspectral remote-sensing reflectance of high-sediment-load waters in the visible to shortwave-infrared domain

ARTICLE *in* APPLIED OPTICS · MARCH 2016

Impact Factor: 1.78 · DOI: 10.1364/AO.55.001738

---

READS

33

5 AUTHORS, INCLUDING:



Zhongping Lee

University of Massachusetts Boston

103 PUBLICATIONS 3,032 CITATIONS

SEE PROFILE

# On the modeling of hyperspectral remote-sensing reflectance of high-sediment-load waters in the visible to shortwave-infrared domain

ZHONGPING LEE,<sup>1,6</sup> SHAOLING SHANG,<sup>2,5</sup> GONG LIN,<sup>2</sup> JUN CHEN,<sup>3</sup> AND DAVID DOXARAN<sup>4</sup>

<sup>1</sup>School for the Environment, University of Massachusetts Boston, Boston, Massachusetts 02125, USA

<sup>2</sup>State Key Lab of Marine Environmental Science, Xiamen University, Xiamen 361005, China

<sup>3</sup>Qingdao Institute of Marine Geology, Qingdao 266071, China

<sup>4</sup>Laboratoire d'Océanographie de Villefranche, UMR 7093, CNRS/UPMC, France

<sup>5</sup>e-mail: slshang@xmu.edu.cn

<sup>6</sup>e-mail: zhongping.lee@umb.edu

Received 13 November 2015; revised 21 January 2016; accepted 21 January 2016; posted 22 January 2016 (Doc. ID 248519); published 1 March 2016

We evaluated three key components in modeling hyperspectral remote-sensing reflectance in the visible to shortwave-infrared (Vis–SWIR) domain of high-sediment-load (HSL) waters, which are the relationship between remote-sensing reflectance ( $R_{rs}$ ) and inherent optical properties (IOPs), the absorption coefficient spectrum of pure water ( $a_w$ ) in the IR–SWIR region, and the spectral variation of sediment absorption coefficient ( $a_{sed}$ ). Results from this study indicate that it is necessary to use a more generalized  $R_{rs}$ –IOP model to describe the spectral variation of  $R_{rs}$  of HSL waters from Vis to SWIR; otherwise it may result in a spectrally distorted  $R_{rs}$  spectrum if a constant model parameter is used. For hyperspectral  $a_w$  in the IR–SWIR domain, the values reported in Kou *et al.* (1993) provided a much better match with the spectral variation of  $R_{rs}$  in this spectral range compared to that of Segelstein (1981). For  $a_{sed}$  spectrum, an empirical  $a_{sed}$  spectral shape derived from sample measurements is found working much better than the traditional exponential-decay function of wavelength in modeling the spectral variation of  $R_{rs}$  in the visible domain. These results would improve our understanding of the spectral signatures of  $R_{rs}$  of HSL waters in the Vis–SWIR domain and subsequently improve the retrieval of IOPs from ocean color remote sensing, which could further help the estimation of sediment loading of such waters. Limitations in estimating chlorophyll concentration in such waters are also discussed. © 2016 Optical Society of America

**OCIS codes:** (010.0010) Atmospheric and oceanic optics; (010.0280) Remote sensing and sensors; (010.1030) Absorption; (010.4450) Oceanic optics; (010.5620) Radiative transfer.

<http://dx.doi.org/10.1364/AO.55.001738>

## 1. INTRODUCTION

Knowledge of the distribution of suspended particulate matters (SPMs) in the water column is important for many applications and ecosystem studies [1–3]. To meet this demand, numerous studies were carried out in past decades to develop remote-sensing algorithms to retrieve the concentration of SPM ([SPM],  $g/m^3$ ) from various satellite measurements [2,4–10]. Since most algorithms are empirical in nature, the applicability of such algorithms is then limited to data or regions with similar characteristics as those used for the algorithm development. To mechanistically understand the spectral variation of water color with high loadings of SPM—a necessity to develop widely applicable algorithms for [SPM] retrieval—there were also a few modeling studies based on radiative transfer [2,3,11,12].

Results from these modeling studies provided in general reasonable qualitative explanations of the spectral variation of remote-sensing reflectance ( $R_{rs}$ ,  $sr^{-1}$ ) in the visible-to-near-infrared (Vis–NIR, 400–900 nm) domain for varying loading of sediments. However, some spectral variations observed in the measured  $R_{rs}$  spectra were not well explained, and the spectral match between measured and modeled  $R_{rs}$  was not uniform across the spectrum [11,12]. At the same time, it has been quite vague regarding the reasons for such spectral-selective closure in  $R_{rs}$  modeling.

A remote sensor, either ship-borne or space-borne, measures total-upwelling radiance ( $L_t$ ), which can be converted to water-leaving radiance ( $L_w$ ) after correcting contributions from the water-surface reflection and path radiance [13–15].  $L_w$  varies

Table 1. Field Sites and Measurements

Sites	Number of Stations	Cruise Time	Properties Measured	Instrument Used
Subei Bank	3	12/24/2008	$R_{rs}$ , $a_{sed}$	GER 1500 (for $R_{rs}$ ); PE Lambda 950 (for $a_{sed}$ )
Upper Changjiang Estuary	2	4/12/2009	$R_{rs}$ , $a_{sed}$	GER 1500 (for $R_{rs}$ ); PE Lambda 950 (for $a_{sed}$ )
Lower Changjiang Estuary	20	10/14/2009	$R_{rs}$	ASD (for $R_{rs}$ )

with both downwelling irradiance (incident light) and water constituents. To separate these two factors, the remote-sensing reflectance ( $R_{rs}$ ) is defined as

$$R_{rs}(\lambda) = \frac{L_w(\lambda)}{E_d(\lambda, 0+)} \quad (1)$$

$R_{rs}$  is an apparent optical property [AOP] [16], which is fundamentally determined by the inherent optical properties [IOP] [16,17] of water constituents, while it also weakly varies with sun angle and viewing angle [18]. Here we examine the key components in modeling hyperspectral  $R_{rs}$  of high-sediment-load (HSL) waters, which refer to those where sediments make significant contributions to the absorption and scattering properties. Specifically, we discuss three important components involved in the theoretical interpretation of spectral  $R_{rs}$  of HSL waters after assuming the power-law function of wavelength is still applicable to the backscattering spectrum of suspended sediments [11,19,20]. These components are (1) the relationship between  $R_{rs}$  and IOPs, (2) the hyperspectral absorption coefficient of pure water ( $a_w$ ,  $m^{-1}$ ) in the NIR–SWIR domain, and (3) the spectral model of sediment absorption coefficient ( $a_{sed}$ ,  $m^{-1}$ ). In particular we extend the spectral coverage to the shortwave-infrared (SWIR) region, as information in these bands is useful for the estimation of SPM concentrations [9] and for the correction of atmospheric contributions for remote sensing of coastal/in-land turbid waters [21,22]. The effort is not intended to develop algorithms for the retrieval of [SPM] or for the correction of atmosphere contributions but rather to improve the bases for better understanding of the spectral variation of  $R_{rs}$  of HSL waters in the Vis–SWIR domain. Such an understanding is important for the development and processing of the next generation of ocean color satellite sensors, including Plankton, Aerosol, and Ocean Ecosystem and Geostationary Coastal and Air Pollution Events. Both are intended to have hyperspectral capabilities covering the Vis–SWIR domain.

## 2. DATA

To evaluate the three components on interpreting hyperspectral remote-sensing reflectance of high-sediment-load waters, both synthetic and field-measured data were used, and the following provides a summary of the datasets.

### A. In Situ Data

*In situ* data obtained from the Subei Bank and the Changjiang (Yangtze) River estuary (see Fig. 1 for locations) were used in this effort, where both locations are famous for high concentrations of sediments due to run-off from the Changjiang River and the resuspension of bottom sediments by tidal currents. Table 1 summarizes the properties measured and used. The measurements of  $R_{rs}$  followed the above-surface approach

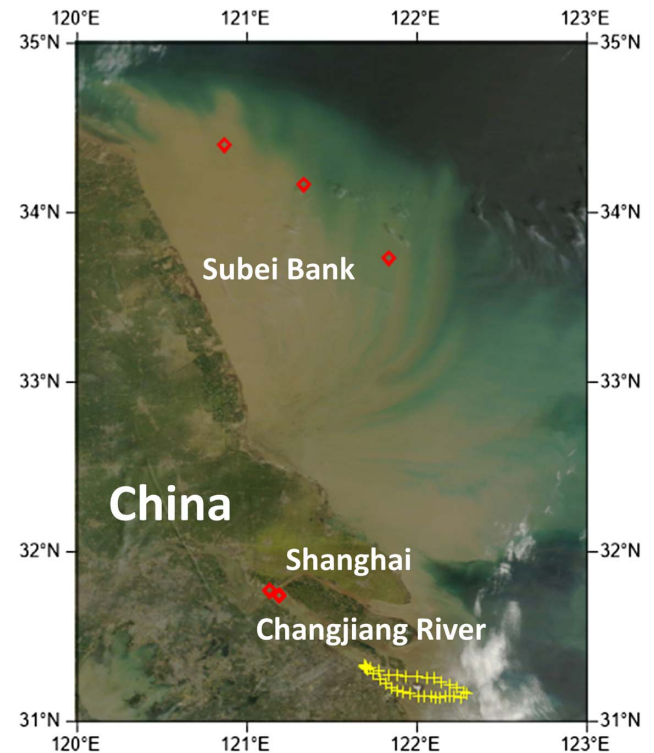


Fig. 1. Location of measurements made in Subei Bank and the Changjiang (Yangtze) River estuary, China. Red diamonds for remote sensing measurements by a GER 1500, while yellow cross for remote sensing measurements by an ASD.

[14,23], i.e., a spectral radiometer was used to measure total above-surface radiance ( $L_t$ , in raw digital counts or in radiometric units), downwelling sky radiance ( $L_{sky}$ ) from the reciprocal angle of measuring  $L_t$ , and radiance leaving a standard gray card ( $L_g$ ).  $R_{rs}$  was then calculated as [15,24,25]

$$R_{rs}(\lambda) = \frac{\rho L_t(\lambda) - FL_{sky}(\lambda)}{\pi L_g(\lambda)} - \Delta, \quad (2)$$

with  $\rho$  the reflectance of the gray card and  $F$  (0.023 and spectrally constant) the Fresnel reflectance of air–sea surface. Note that this processing of calculating  $R_{rs}$  is slightly different from that in Mobley [14], as another parameter ( $\Delta$ ,  $sr^{-1}$ ) is implemented to account for the skylight from other directions that are also reflected into the sensor's field of view by the roughened sea surface [15].  $\Delta$  was considered wavelength independent but varied from measurement to measurement. This extra procedure here is named as a second-order correction. For the measurements in the Subei Bank and the upper mouth of the Changjiang River estuary (the red diamonds in Fig. 1), a GER

1500 spectroradiometer (Spectra Vista Corporation, USA) was used, which covers wavelengths up to 1100 nm, so value of  $\Delta$  was determined by setting the average of  $R_{rs}$  (965–990 nm) to be 0 for each station as the absorption coefficient of pure water reaches a local maximum ( $\sim 50 \text{ m}^{-1}$ ) around this band. For the measurements in the lower mouth of the Changjiang River estuary, an ASD spectroradiometer (ASD Inc., Boulder, CO) was used [26] that covers wavelengths up to 2500 nm. For these measurements, the value of  $\Delta$  for each station was determined by setting the average of  $R_{rs}$  (1600–1650 nm) to be 0, as data in the longer wavelengths became too noisy due to the extremely high absorption of pure water [27]. Figure 2(a) shows an example of  $R_{rs}$  spectra with and without this second-order correction, where  $\Delta$  was  $\sim 0.003 \text{ sr}^{-1}$  for this case, a value about two times the  $R_{rs}$  at 550 nm of oceanic waters [28]. However, because the absorption coefficients in the 1600–1650 nm range are greater than  $1000 \text{ m}^{-1}$ ,  $R_{rs}$  of nearly all natural waters at this band should be hardly detectable [27]. Figure 2(b) presents hyperspectral  $R_{rs}$  spectra from these measurements after applying this second-order correction, where  $R_{rs}$  (815) is in a range of  $0.005\text{--}0.05 \text{ sr}^{-1}$  due to high load of suspended sediments, and the spectral shapes of these  $R_{rs}$  are similar to those in the literature [20,29].

Separately, the absorption coefficient of suspended particles corresponding to the  $R_{rs}$  measurements at the Subei Bank and the upper mouth of the Changjiang River estuary (red symbols in Fig. 1) were measured from surface water samples. As Babin and Stramski [30], the absorption coefficient was measured with a dual-beam PE Lambda 950 spectrophotometer equipped with an integrating sphere (150 mm in diameter) after sample filtration with GF/F filters following the filter-pad technique [31]. Because of the high scattering from the nonpigmented particles, the transmittance–reflectance (T–R) method [32] was followed for the measurements.  $a_{sed}$  was further measured after pigment extraction by methanol [33] with the same T–R scheme, and the final  $a_{sed}$  was obtained after subtracting the lowest value in the near-infrared (800–900 nm) following Babin and Stramski [30]. This procedure might overcorrect  $a_{sed}$  because  $a_{sed}$  is not necessarily negligible in the longer wavelengths [34,35]. But, because this bias is spectrally flat, such an adjustment does not affect the spectral curvature of  $a_{sed}$ . The resulted  $a_{sed}$  at 440 nm was as high

as  $\sim 5.0 \text{ m}^{-1}$ , which suggests equivalent [SPM] as high as  $\sim 500 \text{ g/m}^3$  by assuming a  $0.01 \text{ m}^2/\text{g}$  specific absorption coefficient at 440 nm [30,35,36].

## B. Synthetic Data

Spectral  $R_{rs}$  of waters with [SPM] set as 1, 5, 10, 50, 100, 500, 1000, and 2000  $\text{g/m}^3$  were simulated using Hydrolight (v5.2) [37]. Wavelengths were set in a range of 360 to 990 nm with a 10 nm resolution. In these simulations, the specific absorption coefficient of SPM was set as  $0.001 \text{ m}^2/\text{g}$ , and the specific scattering coefficient of SPM was set as  $0.1 \text{ m}^2/\text{g}$  [38]; both were set as spectrally independent. The phase function for particle scattering was based on Fournier and Forand [39] with a backscattering to scattering ratio of 0.03, a value generally representing scattering of inorganic particles [40,41]. These parameters used in the IOP setups may not match exactly the features of sediment absorption and scattering coefficients [30,35,36,42], but it is appropriate here, as the objective of the simulations is to evaluate the relationship between  $R_{rs}$  and IOPs of any wavelength rather than to have the simulated  $R_{rs}$  spectrum match field-measured  $R_{rs}$ . The simulations, on the other hand, did cover the general range ( $\sim 0$  to  $\sim 0.08 \text{ sr}^{-1}$ ) of  $R_{rs}$  observed in the field [20,26,29]. Further, concentration of chlorophyll ([Chl]) was kept as  $1 \text{ mg/m}^3$  for these simulations, while the absorption of colored dissolved organic matter (CDOM) at 440 nm was kept the same as that of the chlorophyll absorption coefficient at this wavelength, which was simulated following Bricaud *et al.* [43].

## 3. KEY COMPONENTS IN MODELING SEDIMENT-DOMINATED $R_{rs}$

### A. Analytical Model for Remote-Sensing Reflectance

$R_{rs}$  is fundamentally a function of the total absorption ( $a$ ,  $\text{m}^{-1}$ ) and total backscattering ( $b_b$ ,  $\text{m}^{-1}$ ) coefficients of water constituents [17], which can be easily converted from the subsurface remote-sensing reflectance ( $r_{rs}$ ,  $\text{sr}^{-1}$ ), defined as the ratio of upwelling radiance to downwelling irradiance evaluated just below the surface [44]. For easy implementation, there have been generally two  $r_{rs}$ –IOP relationships employed for the interpretation of spectral  $r_{rs}$  of HSL waters and [SPM] retrievals. One is [6,9,26,29]

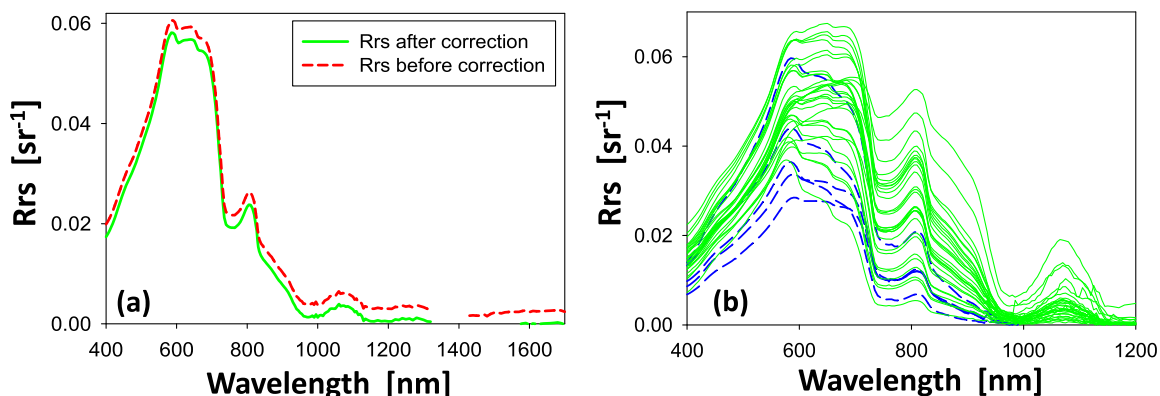


**Fig. 2.** (a) Example of measured remote-sensing reflectance ( $R_{rs}$ ,  $\text{sr}^{-1}$ ) with and without second-order correction. (b)  $R_{rs}$  spectra measured in the Subei Bank and the upper mouth of the Changjiang River estuary (blue curves, the red diamonds in Fig. 1) and the lower mouth of the Changjiang River estuary (green curves, 20 stations).



$$r_{rs}(\lambda) = g_1 \frac{b_b(\lambda)}{a(\lambda) + b_b(\lambda)}, \quad (3)$$

with  $g_1$  a constant. The other one is [12,45]

$$r_{rs}(\lambda) = \frac{R(\lambda)}{Q}, \quad (4a)$$

with

$$R(\lambda) = \frac{b_b(\lambda)/a(\lambda)}{1 + b_b(\lambda)/a(\lambda) + \sqrt{1 + 2b_b(\lambda)/a(\lambda)}}. \quad (4b)$$

Here  $R$  is the subsurface irradiance reflectance, which is defined as the ratio of upwelling irradiance to downwelling irradiance evaluated just below the surface [46,47].  $Q$  is the so-called  $Q$ -factor [18,48], evaluated just below the surface, which is defined as the ratio of upwelling irradiance to upwelling radiance, with a value ranging from  $\sim 3$  to 6 for nadir-looking radiance [18,49].

Equation (3) was approximated oceanic waters [50] where the ratio of scattering to absorption coefficients is generally less than tens [50,51]. This is no longer the case for HSL waters, as this ratio could be as high as hundreds at some wavelengths; consequently it is questionable to apply Eq. (3) to such extreme waters.

The model by Eq. (4), on the other hand, is based on the relationship of subsurface irradiance reflectance [12,45], where the model for  $R$  was developed for scattering media where the upwelling and downwelling irradiances can be considered nearly equal to each other [52,53]. This is consistent qualitatively for HSL waters but should be limited to wavelengths with a high scattering-to-absorption ratio, because this ratio is highly wavelength-dependent for aquatic environments. Further, in the application of the model by Eq. (4), it requires a specification or approximation of the “ $Q$  factor” and was usually taken as a constant [12,45]. This might be generally applicable, as the variation of  $Q$  was found in a small range spectrally for the remote-sensing domain [18,54].

To demonstrate numerically the applicability of both models in simulating remote-sensing reflectance spectrum of HSL waters, a model parameter ( $g$ ) for  $r_{rs}$  is calculated from the Hydrolight simulations,

$$g(\lambda) = \frac{r_{rs}(\lambda)}{u(\lambda)}, \quad (5)$$

with  $u$  the ratio of  $b_b/(a + b_b)$ . Figure 3(a) shows how  $g$  varies with  $u$  for these simulations. As presented in many studies for oceanic waters [18,55–57], the value of parameter  $g$  is not a constant but rather varies over a factor of two between the low and high ends, even for HSL waters. Therefore, if a constant  $g$  value is used to model the  $r_{rs}$  spectrum as shown in Eq. (3), it is likely to overestimate  $r_{rs}$  for low  $u$  (e.g., regions in the SWIR domain) while underestimating  $r_{rs}$  for high  $u$  (e.g., regions in the Vis domain). It is necessary to point out that because remote-sensing reflectance is a measure of the radiance in a specific direction, the value of  $g$  for a  $b_b/(a + b_b)$  ratio depends on the details of the scattering phase function of particles [17,58]. Thus if the phase function used in the Hydrolight simulations is changed, the magnitude of the  $g$  versus  $b_b/(a + b_b)$  dependence will likely change accordingly, but the general trend between  $g$  and  $b_b/(a + b_b)$  will remain.

The equivalent  $g$  value of the  $r_{rs}$  model by Eq. (4) is calculated from the ratio of the modeled  $r_{rs}$  [Eq. (4b)], with the  $Q$  parameter set as 3.25 [45] to  $u$ , and Fig. 3(a) also compares the  $g$  values from this model with the values obtained from Hydrolight simulations. Not too surprisingly, because the model for  $R$  was developed for high-scattering media [52,53], the resulted  $g$  values from Eq. (4) match Hydrolight  $g$  values very well for  $u$  values higher than 0.5 (equivalent scattering-to-absorption ratio is  $\sim 60$ ). But it overestimates Hydrolight  $g$  values by about 80% for  $u$  values less than  $\sim 0.1$  (equivalent scattering-to-absorption ratio is  $\sim 4$ ). This suggests that the model by Eq. (4) works the best for wavelengths (e.g., the green/yellow wavelengths for HSL waters, see Fig. 2) with  $r_{rs}$  (i.e.,  $u$ ) values very high ( $u > \sim 0.5$ ,  $r_{rs} > \sim 0.07 \text{ sr}^{-1}$ ); however, it will likely overestimate the  $r_{rs}$  values by  $\sim 80\%$  for other wavelengths (e.g., the blue or SWIR bands for HSL waters). Because the scattering-to-absorption ratio of oceanic and coastal waters is highly wavelength-dependent and this ratio reaches decades only in some wavelengths of HSL waters, the above results (and the nature of the  $R$  model) indicate that the  $r_{rs}$  model by Eq. (4) is applicable to limited wavelengths associated with limited aquatic environments. This may not be that critical if the focus is to retrieve [SPM] empirically from

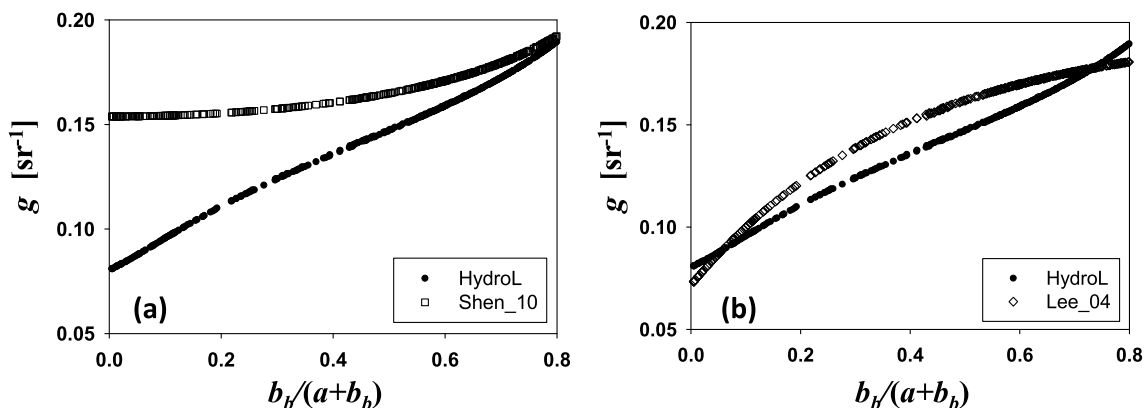


**Fig. 3.** (a) Relationship between  $r_{rs}$ -model coefficient ( $g$ ) and  $b_b/(a + b_b)$  (Shen\_10 for equivalent  $g$  model, Eq. (4), of Shen *et al.* [12,45]). (b) As (a) but between Hydrolight-simulated and Lee *et al.* [60] (Lee\_04) modeled  $g$  [Eq. (6)].

remote-sensing reflectance [9,12], as the empirical algorithm coefficients between  $R_{rs}$  (or  $r_{rs}$ ) and [SPM] may compensate this uncertainty in modeling  $r_{rs}$ .

There are also models developed to explicitly account for the different effects of molecular and particle scatterings [59] in formulating remote-sensing reflectance [57,60], and one of the models used particle-scattering weighted contribution to describe the  $g$  parameter:

$$g(\lambda) = 0.113 \frac{b_{bw}(\lambda)}{b_{bw}(\lambda) + b_{bp}(\lambda)} + 0.197 \left[ 1 - 0.636 \exp \left( -2.552 \frac{b_{bp}(\lambda)}{a(\lambda) + b_b(\lambda)} \right) \right] \times \frac{b_{bp}(\lambda)}{b_{bw}(\lambda) + b_{bp}(\lambda)}, \quad (6)$$

with the constants adopted in Eq. (6) derived by fitting Hydrolight simulations of oceanic waters. Here  $b_{bw}$  and  $b_{bp}$  are the backscattering coefficients of water molecules and suspended particles, respectively. Figure 3(b) compares  $g$  values modeled by Eq. (6) with those from the above Hydrolight simulations for HSL waters. It is found that, although the model of Eq. (6) was developed based on a completely different particle phase function (the average of Petzold [61,62] backscattering efficiency is 1.8%), the  $g$  coefficients modeled by Eq. (6) match the Hydrolight simulations very well (the average difference is 6.2%, and maximum difference is 12.2%). Additionally, they reasonably reflect variation of Hydrolight  $g$  (and thus the spectral variation of  $r_{rs}$  for a given set of IOPs) for the wide range of  $u$  values of HSL waters. The difference in the  $g$  values is a result of different particle scattering phase functions used in the two series of Hydrolight simulations, which highlights the fact that in the practice of remote sensing it measures photons in one specific direction rather than the entire backward-scattered domain and that the exact phase function of particle scattering is not known at the time of taking remote-sensing measurements. Further, compared to the relationship [Fig. 3(b)] between  $g$  and  $b_b/(a + b_b)$  shown in Lee *et al.* [60], there are no obvious multiple  $g$  values for a given  $b_b/(a + b_b)$  value from these simulations. This is because the contribution to  $r_{rs}$  from the water molecule scattering is negligible for HSL waters, and it is simply the phase function of particle scattering that plays the role for all wavelengths.

Because the ~6% error is equivalent to or better than that of *in situ* measurements of AOPs and IOPs and the error is quite uniform for varying  $u$  values, the model by Eq. (6) will be used in the following to assess the impact of different spectral models of  $a_{sed}$  on the interpretation of hyperspectral  $r_{rs}$  and the analytical inversion of IOPs, although other models [56,57] may also be used for this task. The ~6% error of Eq. (6) in modeling  $g$  will affect the accuracy of retrieving  $b_{bp}$  from  $r_{rs}$  because  $r_{rs}$  is generally proportional to  $b_{bp}$ .

## B. Hyperspectral Absorption Coefficient of Pure Water in the NIR–SWIR Domain

Hyperspectral absorption of pure water ( $a_w$ ,  $m^{-1}$ ) is a basic optical property required to model spectral  $r_{rs}$ , and the values of  $a_w$  in the NIR–SWIR are critical to model  $r_{rs}$  in this spectral region, as other water constituents have either insignificant or

negligible contributions. There have been quite many reports regarding  $a_w$  values in the UV-to-Vis domain [63,64], with the latest one derived from the “clearest” natural waters [65]. For  $a_w$  in the NIR–SWIR domain, although the values reported in Hale and Querry [66] have been widely used in atmospheric and oceanic studies [27], values of hyperspectral  $a_w$  are found only in Segelstein [67] and Kou *et al.* [27]. The  $a_w$  values of Segelstein [67] (with a spectral resolution ~5 nm in the NIR domain) were compiled from the literature, while the values of Kou *et al.* [27] (with a spectral resolution ~1 nm in the NIR domain) were measurements of water samples with a Fourier transform infrared spectrometer. These two  $a_w$  spectra in general show very good agreement for the NIR–SWIR domain (see Fig. 4, where S\_81 for Segelstein [67] and K\_93 for Kou *et al.* [27]), but they do show large differences around 750–1100 nm (see Table 2 for values of selected wavelengths). In particular their spectral curvatures are quite different, as evidenced by their spectra of normalized first-order derivative (also see Fig. 4); thus it is useful and important to determine if the later results of Kou *et al.* [27] are indeed a more appropriate  $a_w$  spectrum to model hyperspectral  $r_{rs}$ . We used the normalized first-order derivative (NFD) of a spectrum [ $S(\lambda)$ ] for this analysis, which is defined as

$$NFD_S(\lambda_x) = \frac{S(\lambda_2) - S(\lambda_1)}{S(\lambda_2) + S(\lambda_1)}. \quad (7)$$

Here  $S$  represents a spectrum, and  $\lambda_x$  is the middle wavelength between  $\lambda_1$  and  $\lambda_2$ . Compared to the conventional first-order derivative, it is easier to visualize the curvature changes of  $S(\lambda)$  when values of  $S(\lambda)$  involves several orders of magnitude (such as  $a_w$  from NIR to SWIR bands).

For this evaluation of the  $a_w$  spectra, we compared the NFD spectrum of  $a_w$  with the NFD of  $R_{rs}$  in the 750–1300 nm range, as the spectral shape of  $R_{rs}$  in the NIR–SWIR domain is primarily determined by that of  $a_w$ . For the calculation of NFD of  $R_{rs}$  ( $NFD_{R_{rs}}$ ),  $S(\lambda) = R_{rs}(\lambda)$ . And, to minimize the impact of measurement errors or noises on the calculated spectral

**Table 2. Pure-Water Absorption Coefficients (Units:  $m^{-1}$ ) in the 750–1150 nm Range Used in this Study<sup>a</sup>**

Wavelength (nm)	S_81 $a_w$	K_93 $a_w$
750	2.34	2.47
775	2.21	2.55
800	1.88	2.15
825	2.79	2.57
850	4.45	4.26
875	5.86	5.23
900	7.33	6.88
925	16.19	11.14
950	43.47	32.66
975	52.20	56.58
1000	45.00	48.60
1025	33.06	33.06
1050	21.16	20.96
1075	19.27	18.12
1100	26.02	24.88
1125	48.04	37.69
1150	136.57	133.16

<sup>a</sup>S\_81  $a_w$  is From Segelstein [67] and K\_93  $a_w$  is from Kou *et al.* [27].

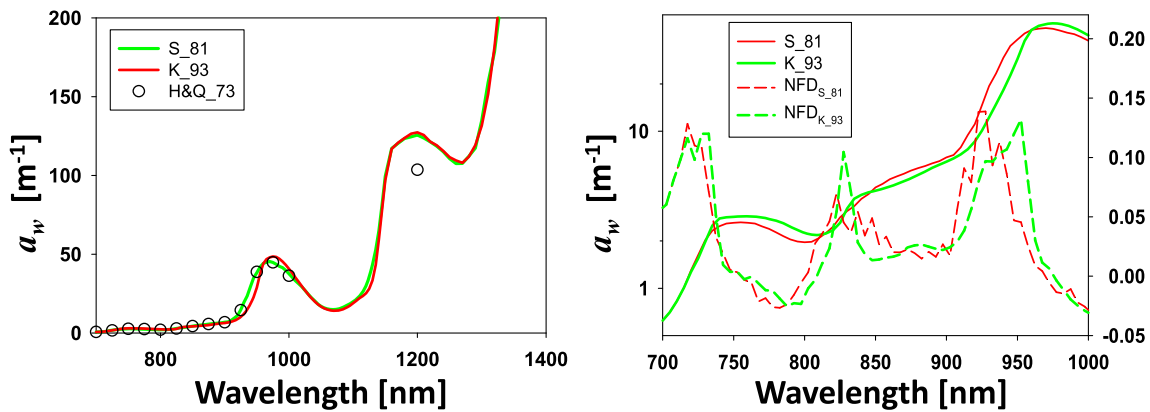


**Fig. 4.** (Left) Absorption coefficients of pure water in the NIR-SWIR domain. S\_81 for the  $a_w$  spectrum of Segelstein [67] and K\_93 for the  $a_w$  spectrum of Kou *et al.* [27]. H&Q\_73 for the  $a_w$  spectrum of Hale and Query [66]. (Right)  $a_w$  spectra of S\_81 and K\_93 for the 700–1000 nm range, along with their normalized first-order derivatives (right axis), respectively.

curvature, spectrally smoothed  $R_{rs}(\lambda)$  of remote-sensing reflectance with  $R_{rs}(1060) > 0.005 \text{ sr}^{-1}$  (a total of eight stations with [SPM]  $> 170 \text{ g/m}^3$ ) were used, and the average spectrum of the 8 NFD $_{R_{rs}}$  is presented in Fig. 5 and used in subsequent statistical analysis. For the comparison of  $a_w$  curvature with  $R_{rs}$  curvature, because  $R_{rs}$  is inversely proportional to  $a_w$ ,  $S(\lambda) = 1/a_w(\lambda)$  was used and the resulted NFD of each absorption spectrum is represented as NFD $_{1/a_w}$ . Figure 5 compares the averaged NFD $_{R_{rs}}$  with NFD $_{1/a_w}$  of the two hyperspectral  $a_w(\lambda)$ . Clearly NFD $_{1/K_{93}}$  matches NFD $_{R_{rs}}$  much better, where the coefficient of determination ( $R^2$ ) between NFD $_{R_{rs}}$  and NFD $_{1/K_{93}}$  is 0.84 for the spectral window of 750–1300 nm (700–750 nm range was excluded due to stronger influences of other water constituents of HSL waters), while it is 0.67 between NFD $_{R_{rs}}$  and NFD $_{1/S_{81}}$ . In particular, both NFD $_{R_{rs}}$  and NFD $_{1/K_{93}}$  show values as 0 at  $\sim 810 \text{ nm}$ , indicating a match between local maximum of  $R_{rs}$  and local minimum of  $a_w$ . In addition to the lower correlation between NFD $_{R_{rs}}$  and NFD $_{1/S_{81}}$ , there are a few zig-zags in NFD $_{1/S_{81}}$  for wavelengths in the  $\sim 820$ – $900 \text{ nm}$  range, indicating a result of nonsmoothness of  $a_{w-S_{81}}$  from compilations of  $a_w$  values from sources of courser spectral resolutions

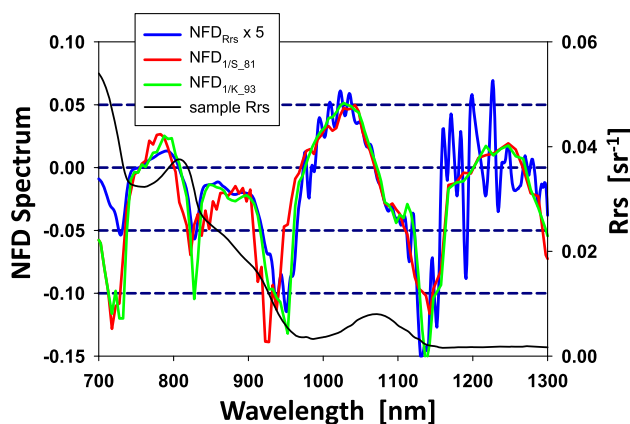


**Fig. 5.** Comparison of spectral curvature (represented by the spectrum of normalized first-order derivative) between  $a_w$  spectrum and  $R_{rs}$  spectrum (see text for details). Also included is an  $R_{rs}$  spectrum (right axis) of high-sediment-load waters.

[67]. These results support the  $a_w$  values of Kou *et al.* [27] for hyperspectral modeling of  $r_{rs}$  of HSL waters in the NIR-SWIR domain. We therefore formed a hyperspectral (400–1350 nm, 5 nm resolution)  $a_w$  spectrum by combining the  $a_w$  values in Lee *et al.* [65] for 350–545 nm, Pope and Fry [63] for 550–720 nm, and Kou *et al.* [27] for 725–2500 nm. This  $a_w$  spectrum was then employed in the following studies.

### C. Spectral Model of Sediment Absorption Coefficient and its Impact on $R_{rs}$ Modeling

#### 1. Spectral Feature of $a_{sed}$

For HSL waters, unlike most marine environments, the absorption coefficient of suspended sediments [ $a_{sed}(\lambda)$ ] dominates the total absorption coefficient for the visible spectral domain; thus the quality in modeling spectral  $a_{sed}$  will have a significant impact on the interpretation of hyperspectral  $R_{rs}$ . Traditionally, a default and standard practice is to express spectral  $a_{sed}$  as an exponential-decay function of wavelength [42,68–70] with or without a positive offset [71]:

$$a_{sed}(\lambda) = a_{sed}(440)e^{-S_{sed}(\lambda-440)}, \quad (8)$$

and the spectral slope ( $S_{sed}, \text{nm}^{-1}$ ) is generally in a range of 0.003–0.011  $\text{nm}^{-1}$  [30,36,68]. However, as demonstrated in Fig. 6 where the average (along with standard deviation) of measured  $a_{sed}$  spectral shapes is presented,  $a_{sed}$  spectrum of HSL waters does not necessarily follow the exponential decay function as commonly adopted [30]. Likely due to its terrigenous origin [30,42,71], it rather shows at least three segments for the 400–800 nm range, with each segment having its own decrease rate with the increase of wavelength. The two inflection points of the three segments are around 430 and 560 nm, and such spectral features in  $a_{sed}(\lambda)$  are also presented in the measured spectra shown in Babin *et al.* [42], Babin and Stramski [30], Astoreca *et al.* [36], Estapa *et al.* [71], and Rottgers *et al.* [35], which indicates that it is not an isolated phenomenon of waters in the Subei Bank and the upper mouth of the Changjiang River estuary. This special spectral feature of  $a_{sed}$  can be further highlighted by comparing the NFD of the measured  $a_{sed}$  spectrum with the NFD of an exponential decay function (also shown in Fig. 6). For an exponential decay function, its NFD spectrum is spectrally flat; but the NFD spectra of the

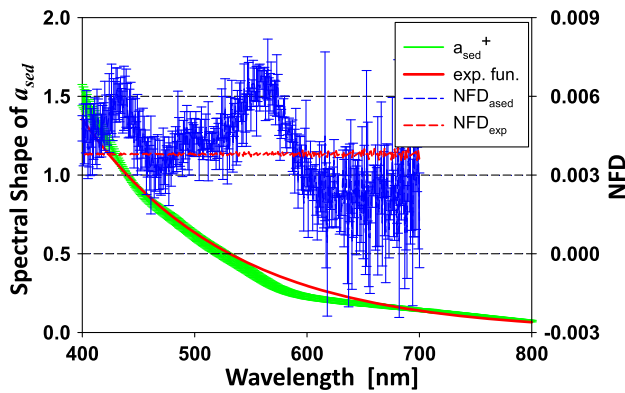


**Fig. 6.** Spectral shape (left axis, green curves; average and standard deviation from five stations) of measured sediment absorption coefficient ( $a_{\text{sed}}$ , normalized at 440 nm), and an exponential-decay function (red curve) with an exponential component as  $0.0076 \text{ nm}^{-1}$ . Also included are the NFD spectra (right axis) of measured  $a_{\text{sed}}$  (blue curves) and that of the exponential model (red dashed line). NFD spectrum (average and standard deviation) of measured  $a_{\text{sed}}$  is truncated at 700 nm, as it is too noisy for the longer wavelengths.

measured  $a_{\text{sed}}$  show quite distinctive spectral characteristics with two pronounced local maxima at  $\sim 430 \text{ nm}$  and  $\sim 560 \text{ nm}$ . Because of this complex spectral variation, a mathematical function like Eq. (8) cannot accurately describe the wavelength dependence of  $a_{\text{sed}}$ , and this inaccuracy has significant consequences on the analytical inversion of  $R_{\text{rs}}$  as demonstrated below.

## 2. Impact of Spectral $a_{\text{sed}}$ Model on $R_{\text{rs}}$ Inversion

To assess the impact of  $a_{\text{sed}}$  spectral variation on the modeling of  $R_{\text{rs}}$  spectrum and the inversion of IOPs from an  $R_{\text{rs}}$  spectrum, two schemes to model  $a_{\text{sed}}$  spectrum were implemented to invert  $R_{\text{rs}}$ . As described by Eq. (3), spectral  $r_{\text{rs}}$  (and then  $R_{\text{rs}}$ ) is a function of both spectral  $a$  and spectral  $b_b$ . Following conventional practices [11,70], the total absorption coefficient ( $a$ ) is expressed as

$$a = a_w + a_{\text{ph}} + a_y + a_{\text{sed}}, \quad (9)$$

with  $a_{\text{ph}}$  and  $a_y$  the absorption coefficients of phytoplankton and yellow substance, respectively.  $a_{\text{ph}}(\lambda)$  is expressed as [70]

$$a_{\text{ph}}(\lambda) = a_{\text{ph}}(440)a_{\text{ph}}^+(\lambda), \quad (10)$$

and the spectral shape of phytoplankton absorption coefficient,  $a_{\text{ph}}^+(\lambda)$ , was obtained from IOCCG Report #5 [70] with a corresponding  $a_{\text{ph}}(440)$  as  $0.1 \text{ m}^{-1}$  (equivalent [Chl] is  $\sim 3 \text{ mg/m}^3$ ). Further,  $a_{\text{ph}}^+(\lambda)$  for wavelengths longer than 800 nm is considered the same as  $a_{\text{ph}}^+(800)$ .

Spectral  $a_y$  is expressed following Bricaud *et al.* [72]:

$$a_y(\lambda) = a_y(440)e^{-S_y(\lambda-440)}, \quad (11)$$

with the exponent constant ( $S_y$ ,  $\text{nm}^{-1}$ ) taken as  $0.0176 \text{ nm}^{-1}$  [42].

Because phytoplankton and water molecules have negligible contributions to the scattering processes of sediment-dominated waters, the total backscattering coefficient ( $b_b$ ) is essentially those from the suspended sediments ( $b_{b-\text{sed}}$ )

$$b_b = b_{b-\text{sed}}. \quad (12)$$

Spectral  $b_{b-\text{sed}}$  is further expressed as [11,19,38]

$$b_{b-\text{sed}}(\lambda) = X \left( \frac{440}{\lambda} \right)^Y, \quad (13)$$

with parameter  $X$  representing  $b_{b-\text{sed}}$  at 440 nm and  $Y$  for the power coefficient of the  $b_{b-\text{sed}}$  spectrum.

Two schemes were used separately to model the spectral variation of  $a_{\text{sed}}$ :

Scheme A: As usual [11,68,70,71], the spectral dependence of  $a_{\text{sed}}$  is modeled as Eq. (8), i.e., an exponential-decay function of wavelength with two free variables [ $a_{\text{sed}}(440)$  and  $S_{\text{sed}}$ ] to describe the spectral variation of  $a_{\text{sed}}$ .

Scheme B: The spectral variation of  $a_{\text{sed}}$  is modeled as

$$a_{\text{sed}}(\lambda) = A_{\text{sed}}(440)a_{\text{sed}}^+(\lambda) + B_{\text{sed}}, \quad (14)$$

with  $a_{\text{sed}}^+$  an averaged spectral shape of  $a_{\text{sed}}(\lambda)$  instead of an exponential decay function of wavelength, which is defined as  $a_{\text{sed}}(\lambda)$  normalized to  $a_{\text{sed}}(440)$ .  $a_{\text{sed}}^+$  was derived from measurements made in waters of the Subei Bank and the upper mouth of the Changjiang River estuary (the diamonds of Fig. 1), and this averaged spectral shape is presented in Table 3. The added variable ( $B_{\text{sed}}$ ) is spectrally flat, which basically accounts for the positive offset at the NIR wavelength [71] and the variations in the steepness of  $a_{\text{sed}}(\lambda)$ . Therefore, compared to Eq. (8), the spectral variation of  $a_{\text{sed}}$  is also modeled with two free variables ( $A_{\text{sed}}$  and  $B_{\text{sed}}$ ) to represent both changing magnitude and steepness for different loading and likely compositions of sediments. In addition, this model reflects the observations that  $a_{\text{sed}}$  is not negligible in the NIR wavelengths [35,36,71].

There are thus six variables [ $a_{\text{ph}}(440)$ ,  $a_y(440)$ ,  $a_{\text{sed}}(440)$ ,  $S_{\text{sed}}$ ,  $X$ , and  $Y$  for Scheme A;  $a_{\text{ph}}(440)$ ,  $a_y(440)$ ,  $A_{\text{sed}}$ ,  $B_{\text{sed}}$ ,  $X$ , and  $Y$  for Scheme B] to model an  $R_{\text{rs}}$  spectrum from the visible to NIR–SWIR domain after these modeling steps. To numerically derive the values of these variables for a given  $R_{\text{rs}}$  spectrum, an objective function between modeled and measured  $R_{\text{rs}}$  is defined as

$$\text{obj}_{R_{\text{rs}}} = \sqrt{N} \frac{\sqrt{\sum_{\lambda_S}^{\lambda_L} (R_{\text{rs}}^{\text{mod}} - R_{\text{rs}}^{\text{mea}})^2}}{\sum_{\lambda_S}^{\lambda_L} R_{\text{rs}}^{\text{mea}}}, \quad (15)$$

with  $N$  the total number of wavelengths used in the calculation.  $\text{obj}_{R_{\text{rs}}}$  provides a quantitative measure of spectrally averaged absolute relative difference between modeled and measured  $R_{\text{rs}}$  for the Vis–SWIR domain. The wavelengths of the short end ( $\lambda_S$ ) and the long end ( $\lambda_L$ ) depend on valid  $R_{\text{rs}}$  measurements. For measurements made by a GER 1500 instrument for waters in the Subei Bank and the upper mouth of the Changjiang River estuary (the red diamonds in Fig. 1), this range is 400–950 nm. Values of the six variables could then be derived by minimizing  $\text{obj}_{R_{\text{rs}}}$ , i.e., so-called spectral optimization [73,74]. For HSL waters, because of the limited (5% or less) contributions of  $a_{\text{ph}}$  and  $a_y$  to the total absorption coefficient [2,26,29], values of  $a_{\text{ph}}(440)$  and  $a_y(440)$  could not be well derived from such an optimization process. Therefore, their values were determined *a priori* [both  $a_{\text{ph}}(440)$  and  $a_y(440)$  were fixed as  $0.1 \text{ m}^{-1}$  for all measurements in this study] based on general knowledge of the research regions, and four parameters [ $a_{\text{sed}}(440)$ ,  $S_{\text{sed}}$ ,  $X$ , and  $Y$  for Scheme A;  $A_{\text{sed}}$ ,



**Table 3.** 440-nm Normalized  $a_{\text{sed}}$  Spectrum

Wavelength (nm)	$a_{\text{sed}}^+$
400	1.510
410	1.379
420	1.254
430	1.126
440	1.000
450	0.903
460	0.832
470	0.777
480	0.726
490	0.670
500	0.614
510	0.563
520	0.517
530	0.471
540	0.428
550	0.381
560	0.335
570	0.295
580	0.264
590	0.241
600	0.224
610	0.213
620	0.203
630	0.196
640	0.189
650	0.181
660	0.174
670	0.166
680	0.159
690	0.152
700	0.145
710	0.138
720	0.131
730	0.123
760	0.102
770	0.095
780	0.088
790	0.080
800	0.072
810	0.065
820	0.058
830	0.051
840	0.044
850	0.037
860	0.030
870	0.022
880	0.015
890	0.008
900	0.001

$B_{\text{sed}}$ ,  $X$ , and  $Y$  for Scheme B] were left for the optimization process. This reduction in number of variables also improves derivation efficiency and limits the digital compensation between  $a_y$  and  $a_{\text{sed}}$  because both decrease rapidly with the increase of wavelength. The initial values for the four parameters were set as (2.0, 0.005, 1.0, 0.1 for Scheme A and 2.0, 0.1, 1.0, 0.1 for Scheme B), and the optimizer used for this optimization process is the Solver included in the MS Excel [75].

After the optimization is achieved (i.e.,  $\text{obj}_{\text{Rrs}}$  is minimized), the spectrum of absolute relative difference between measured and modeled  $R_{\text{rs}}$  ( $\text{Dif}_{\text{Rrs}}$ ) of each station is calculated as

$$\text{Dif}_{\text{Rrs}}(\lambda) = 2 \frac{\text{abs}(R_{\text{rs}}^{\text{mod}}(\lambda) - R_{\text{rs}}^{\text{mea}}(\lambda))}{(R_{\text{rs}}^{\text{mod}}(\lambda) + R_{\text{rs}}^{\text{mea}}(\lambda))}. \quad (16)$$

$\text{Dif}_{\text{Rrs}}$  thus provides a measure of the spectral fitness between modeled and measured  $R_{\text{rs}}$  spectra and places equal weightings on both measured and modeled  $R_{\text{rs}}$  spectra for the evaluation of  $\text{Dif}_{\text{Rrs}}$ . Figure 7 presents the averaged  $\text{Dif}_{\text{Rrs}}$  spectrum (and standard deviation) for the measurements of HSL waters in the Subei Bank and upper mouth of the Changjiang River estuary (a total of five stations) when Scheme A was used to model the  $a_{\text{sed}}$  spectrum. It is found that this difference is generally about 3%–7% for the visible domain, similar as results of earlier studies [11].  $\text{Dif}_{\text{Rrs}}$  is ~5% for wavelengths shorter than 420 nm, which could be due to imperfect removal of surface reflected skylight [15,76] and/or imperfect parameterizations of both  $a_y$  and  $a_{\text{sed}}$ .  $\text{Dif}_{\text{Rrs}}$  values are higher for wavelengths in the NIR region (700–900 nm), which are generally due to (1)  $R_{\text{rs}}$  values are generally lower in these bands, so the ratio to a lower value could easily result in higher relative difference and (2) because of the lower  $R_{\text{rs}}$  value in these bands, these wavelengths have relatively lower weighting on  $\text{obj}_{\text{Rrs}}$ ; therefore the numerical solution process will try to focus more on wavelengths having higher  $R_{\text{rs}}$  values. A quite unique output from this scheme is that  $\text{Dif}_{\text{Rrs}}$  is not uniform spectrally in the visible domain similarly, as shown in Doxaran *et al.* [11]; it shows four wide-width (~100 nm) bands of higher  $\text{Dif}_{\text{Rrs}}$  values, indicating spectrally selective matching rather than uniform matching across the spectral range. This spectrally selective feature is further presented in Fig. 8 where examples of “matched”  $R_{\text{rs}}$  spectra are presented, and this limited closure is pronounced for the ~500–700 nm range.

Because Eq. (8) cannot accurately describe the spectral feature of  $a_{\text{sed}}$ , it also resulted in a mismatch between modeled and measured  $a_{\text{sed}}$  spectra, indicating a large difference in the optimization derived spectral  $a_{\text{sed}}$  [see Fig. 8(b) and Fig. 9].  $\text{Dif}_{\text{ased}}$  represents the absolute relative difference between the measured and the retrieved  $a_{\text{sed}}(\lambda)$  defined similarly as quantifying the fitness between the measured and the modeled spectral  $R_{\text{rs}}$ ,

$$\text{Dif}_{\text{ased}}(\lambda) = 2 \frac{\text{abs}(a_{\text{sed}}^{\text{mod}}(\lambda) - a_{\text{sed}}^{\text{mea}}(\lambda))}{(a_{\text{sed}}^{\text{mod}}(\lambda) + a_{\text{sed}}^{\text{mea}}(\lambda))}. \quad (17)$$

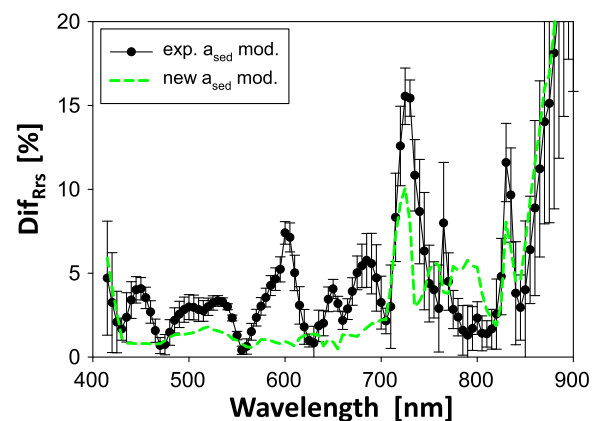


**Fig. 7.** Comparison of  $\text{Dif}_{\text{Rrs}}$  between the two schemes to model  $a_{\text{sed}}$  spectrum.

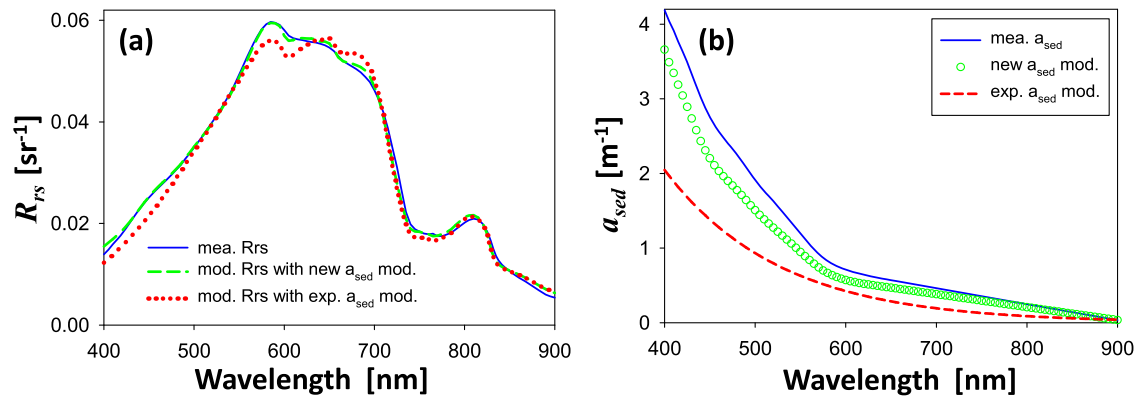


**Fig. 8.** (a) Example of optimized  $R_{rs}$  compared with measured  $R_{rs}$  spectrum, with the two schemes to model the  $a_{sed}$  spectrum. (b) Resulted  $a_{sed}$  spectrum compared to the measured  $a_{sed}$ .

For this evaluation, because initially the measured  $a_{sed}$  spectrum was biased to 0 for the 800–900 nm range and it is known that  $a_{sed}$  values in the NIR are not exactly zero [32,35], the spectrum of  $a_{sed}^{mea}$  used in Eq. (17) was positively biased to match that of  $a_{sed}^{mod}$  at 900 nm, in a way to overcome the uncertainties in scattering correction during  $a_{sed}$  measurements and processing. For the spectral range of 400–800 nm, the averaged  $\text{Dif}_{ased}$  values are  $\sim 30$ –60% when Scheme A was used to describe the  $a_{sed}$  spectrum, and again this difference is spectrally selective. This result is not so surprising due to the fact that Eq. (8) cannot accurately describe the spectral variation of  $a_{sed}$  for such constituents. These results highlight that the use of an exponential function will not result in agreement in spectral curvature between measured and modeled  $R_{rs}$  spectra [see Fig. 8(a) for an example] for such waters, which further affects the retrieval of IOPs.

On the other hand, when Scheme B was employed to describe the  $a_{sed}$  spectrum, we see significantly improved results in the fitness of both  $R_{rs}$  and  $a_{sed}$  spectra (see Figs. 7–9). With the new  $a_{sed}$  model (also two free variables as that in Scheme A), value of  $\text{Dif}_{Rrs}$  is around 2% in the visible domain and generally uniform across the spectral range, indicating a close fitness between modeled and measured  $R_{rs}$  for the Vis–NIR spectral domain. Again, values of  $\text{Dif}_{Rrs}$  are higher for the

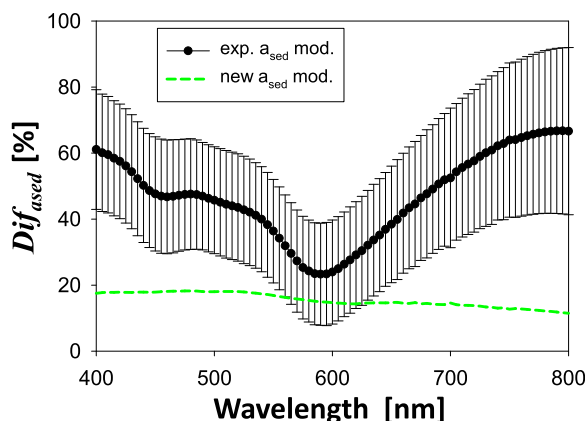


**Fig. 9.** Comparison of  $\text{Dif}_{ased}$  between the two schemes to model  $a_{sed}$  spectrum.

800–950 nm range, a result of generally low  $R_{rs}$  values in these spectral regions (see above). More importantly, in addition to the better fitness of the  $R_{rs}$  spectrum, much better results were achieved in the retrieved  $a_{sed}$  [ $a_{sed}(440)$  in a range of 2.1–4.5  $\text{m}^{-1}$ ] where the averaged  $\text{Dif}_{ased}$  is generally  $\sim 16\%$  ( $\pm \sim 10\%$ ) and no significant spectral variation (see Fig. 9). This result indicates very good agreement between the retrieved and measured  $a_{sed}$  spectra for such extreme conditions, as there are always non-negligible uncertainties in both measured  $R_{rs}$  and  $a_{sed}$  spectra [35,77,78]. It is necessary to point out that as usual a power-law function of wavelength [Eq. (13)] has been used to model the spectrum of particle backscattering coefficient [6,19], which may or may not be exactly the case for the various organic and inorganic particulates in aquatic environments. Further improvements on the closure of  $R_{rs}$  modeling are expected after hyperspectral measurements of  $b_{bp}$  are available.

In short, the mismatch in spectral curvature of  $a_{sed}$  by Eq. (8) not only affects the interpretation of hyperspectral  $R_{rs}$  in the visible–IR domain but also the retrieval of  $a_{sed}$  from  $R_{rs}$  via spectral optimization. This mismatch spills to particle backscattering coefficient and then total absorption coefficient (see Fig. 10), where  $b_{bp}(440)$  could differ by a factor of two in order to achieve a minimized  $\text{obj}_{Rrs}$  (and still much higher  $\text{obj}_{Rrs}$  values compared to Scheme B, see Fig. 7) between modeled and measured  $R_{rs}$  spectra. These results highlight the importance in accurately modeling  $a_{sed}$  spectrum of HSL waters for analytical interpretation and inversion of such waters.

### 3. Test of the New $a_{sed}$ Model with Measurements at Other Areas

This contrast in modeling  $a_{sed}$  spectrum of HSL waters and its application in  $R_{rs}$  inversion were further applied to  $R_{rs}$  data independently measured at the lower mouth of the Changjiang River estuary (the yellow plus in Fig. 1, a total of 20 stations with [SPM] in a range of  $\sim 7$ –700  $\text{g}/\text{m}^3$ ) and the Gironde estuarine (a total of 6 stations, see Doxaran *et al.* [29] for locations), where [SPM] was in a range of  $\sim 6$ –1700  $\text{g}/\text{m}^3$ . Data samples in the Gironde Estuary were selected from numerous field measurements carried out between 1996 and 2001. They correspond to clear blue sky and quasi-plane water surface conditions and are representative for different tidal conditions

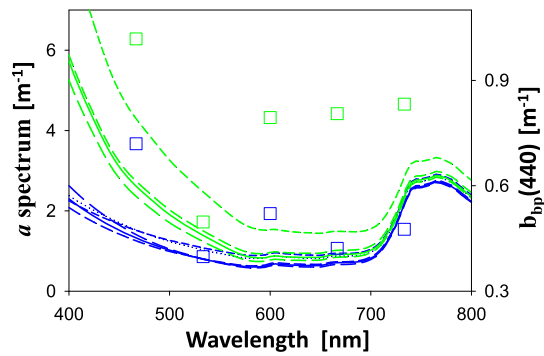


**Fig. 10.** Comparison of optimization derived  $a(\lambda)$  and  $b_{bp}(440)$  between the two schemes to model  $a_{sed}$  spectrum. Blue color lines for results with the exponential  $a_{sed}$  model; green color lines for results with the new  $a_{sed}$  model. Note that  $b_{bp}(440)$  (the squares) values are not spectra but rather the values of the five stations taken in Subei Bank and the upper mouth of the Changjiang River estuary.

(neap–spring tides) and of different river-flow conditions. All the modeling and inversion procedure are the same as applied to measurements made in the Subei Bank, except  $\lambda_L$  was changed to 1350 nm for measurements made at the lower mouth of the Changjiang River estuary by an ASD. Figure 11 compares  $Dif_{Rrs}$  spectrum between Schemes A and B for these measurements, and again, much better fitness (especially for measurements at the lower mouth of the Changjiang River estuary) was achieved with Scheme B to model the spectral variation of  $a_{sed}$  for these waters. Unfortunately, there were no concurrent sample measurements of  $a_{sed}$  to further evaluate the  $a_{sed}$  retrievals. These results suggest a likely broad application of the  $a_{sed}$  spectral shape (Table 3) and the new  $a_{sed}$  model (Eq. 14) for HSL waters.

#### 4. SENSING CHLOROPHYLL CONCENTRATION IN HSL WATERS FROM $R_{rs}$

For the retrieval of a constituent from an  $R_{rs}$  spectrum, it is critical for this constituent to have adequate spectral signature in  $R_{rs}$ . As an example, Fig. 12 shows simulated hyperspectral  $R_{rs}$  spectra for HSL waters by artificially adding more spectral information

of phytoplankton (represented by Chl). For this water where  $a_{sed}(440)$  is  $\sim 4.0 \text{ m}^{-1}$  and  $b_{bp}(440)$  is  $\sim 1.5 \text{ m}^{-1}$ , a change of [Chl] from 0.1 to 10  $\text{mg/m}^3$  [ $a_{ph}(440)$  changed from 0.01 to  $0.2 \text{ m}^{-1}$ ] resulted in almost no change in the modeled  $R_{rs}$  spectra (the green lines). This is not surprising due to  $a_{ph}$  contributing less than 5% of the total absorption coefficient across the visible domain if  $a_{ph}(440) < 0.2 \text{ m}^{-1}$ . A visible change in  $R_{rs}$  spectrum with the increase of [Chl] is the dip around 675 nm, especially when [Chl] becomes much higher ( $> 50 \text{ mg/m}^3$  for this case). If a three-band ratio [79,80] defined as

$$Dip_{Chl} = \frac{R_{rs}(650) \times R_{rs}(705)}{R_{rs}(675)^2} \quad (18)$$

is used to quantify this dip, it is found that  $Dip_{Chl}$  is generally  $< \sim 1.0$  and nearly a constant for  $a_{ph}(440) < 0.2 \text{ m}^{-1}$  (equivalent to [Chl]  $\sim 10 \text{ mg/m}^3$ ) for this case.  $Dip_{Chl}$  increases to 3.1 for  $a_{ph}(440)$  increased to  $5.0 \text{ m}^{-1}$  (equivalent to [Chl]  $\sim 2000 \text{ mg/m}^3$ ). Thus this  $Dip_{Chl}$  could be used as a messenger to indicate detectable phytoplankton in HSL waters. It is found that for all data used in this study (a total of 31 stations), although the variation of  $R_{rs}(860)$  is in a range of  $\sim 0.002\text{--}0.04 \text{ sr}^{-1}$  ( $b_{bp}(440)$  in a range of  $\sim 0.5\text{--}5.0 \text{ m}^{-1}$ , [SPM] in a range of  $\sim 6\text{--}1700 \text{ g/m}^3$ ), values of  $Dip_{Chl}$  are less than 1.0. These results highlight the daunting challenge to accurately retrieve information of chlorophyll concentration (phytoplankton) in HSL waters from passive remote sensing [80], even if we have a perfect  $R_{rs}$  spectrum from any remote-sensing platform, although it could be successful to retrieve [Chl] in highly productive waters [81,82] or where the relative contribution of  $a_{ph}$  is higher. Thus likely the only environmental information that could be well retrieved from  $R_{rs}$  of HSL waters will be the loading of suspended sediments, as has been demonstrated in numerous studies [3,4,29,83,84]. This is not a surprising finding, though, as fundamentally for sediment-dominated waters, due to the significantly reduced availability of light, it is not an ideal condition for phytoplankton to grow in the upper water column, maybe except for the surface skin layer. Consequently, the design of an ocean color satellite sensor could relax its requirement for observations of such waters.

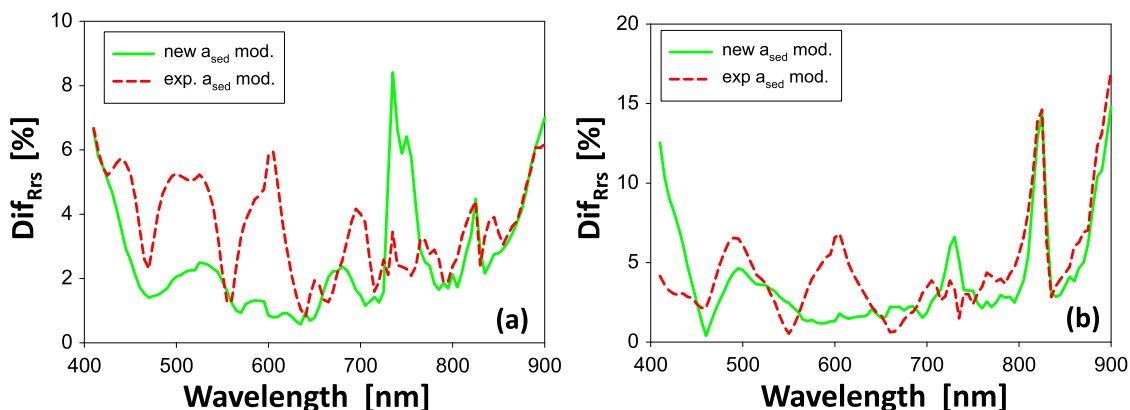


**Fig. 11.** Comparison of  $Dif_{Rrs}$  between the two schemes to model  $a_{sed}$  spectrum for measurements made in other areas. (a) Lower mouth of the Changjiang River estuary (obj<sub>Rrs</sub> for 400–1350 nm). (b) The Gironde estuary.

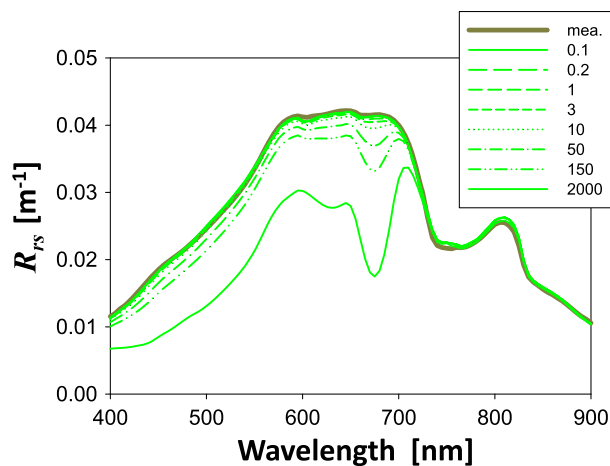


**Fig. 12.** Measured and modeled hyperspectral  $R_{rs}$  spectra for varying amount of phytoplankton in HSL waters. Numbers in the box indicate likely chlorophyll concentration ( $\text{mg}/\text{m}^3$ ).

## 5. CONCLUSIONS

It is well known that the model parameter ( $g$ ) of remote-sensing reflectance of oceanic waters is not a constant for varying water constituents and varying wavelengths, and the results here further highlight that it is necessary to use a more generalized  $r_{rs}$ -IOP model to describe the spectral variation of  $r_{rs}$  of HSL waters; otherwise it may result in a spectrally distorted  $r_{rs}$  spectrum if a constant model parameter is used. In addition, to describe the spectral variation of  $r_{rs}$  in the IR-SWIR domain,  $a_w$  measured by Kou *et al.* [27] would provide a much better match with the spectral variation of  $r_{rs}$ . More importantly, both field measurements of  $a_{sed}$  spectra and modeling of hyperspectral  $r_{rs}$  indicate that the  $a_{sed}$  spectrum of HSL waters does not necessarily follow the commonly used exponential-decay function with the increase of wavelength. Consequently the use of such a function would result in lower quality in  $r_{rs}$  closure and higher uncertainty in the derived IOPs from spectral optimization. This is because for HSL waters,  $a_{sed}$  plays a dominant role in modulating the total absorption spectrum and then the spectral shape of  $r_{rs}$ . The empirical  $a_{sed}$  spectral shape derived from sample measurements, on the other hand, is found working very well in interpreting hyperspectral  $r_{rs}$  for a wide range of waters, which further improves the semi-analytical retrieval of IOPs from an  $r_{rs}$  spectrum. This empirical model for  $a_{sed}$  spectrum might be also applicable for waters with fewer loadings of sediments, because the impact of  $a_{sed}$  to the total absorption will be less significant for such cases, although the model may not be that accurate spectrally. On the other hand, the spectral signatures in both  $a_{sed}$  and  $r_{rs}$  are likely indicators of the terrigenous origin of such sediments. Further, as would be expected, there is no or very limited detectable information of phytoplankton in  $r_{rs}$  spectrum for HSL waters. These results improve our understanding of the spectral variation of  $r_{rs}$  of HSL waters and the potentials and limitations of passive remote sensing of such waters.

**Funding.** National Aeronautics and Space Administration (NASA) (NNX14AQ47A, NNX14AR65G); National

Oceanic and Atmospheric Administration (NOAA) (DG133E-12-SE-1931); National Natural Science Foundation of China (NSFC) (41376177, Shang); Ministry of Science and Technology of China (2013BAB04B00, Shang), Natural Science Foundation of China (41401597, Chen).

## REFERENCES

1. F. T. Manheim and J. C. Hathaway, "Suspended matter in surface waters of the northern Gulf of Mexico," *Limnol. Oceanogr.* **17**, 17–27 (1972).
2. D. Doxaran, J.-M. Froidefond, S. Lavender, and P. Castaing, "Spectral signature of highly turbid waters: application with SPOT data to quantify suspended particulate matter concentrations," *Remote Sens. Environ.* **81**, 149–161 (2002).
3. K. Ruddick, F. Ovidio, D. Van den Eynde, and A. Vasilkov, "The distribution and dynamics of suspended particulate matter in Belgian coastal waters derived from AVHRR imagery," in *9th Conference on Satellite Meteorology and Oceanography*, Paris, France, 1998.
4. A. G. Dekker, R. J. Vos, and S. W. M. Peters, "Analytical algorithms for lake water TSM estimation for retrospective analyses of TM and SPOT sensor data," *Int. J. Remote Sens.* **23**, 15–35 (2002).
5. T. W. Cui, J. Zhang, S. Groom, L. Sun, T. Smyth, and S. Sathyendranath, "Validation of MERIS ocean-color products in the Bohai Sea: a case study for turbid coastal waters," *Remote Sens. Environ.* **114**, 2326–2336 (2010).
6. B. Nechad, K. G. Ruddick, and Y. Park, "Calibration and validation of a generic multisensor algorithm for mapping of total suspended matter in turbid waters," *Remote Sens. Environ.* **114**, 854–866 (2010).
7. G. Neukermans, K. Ruddick, E. Bernard, D. Ramon, B. Nechad, and P. Y. Deschamps, "Mapping total suspended matter from geostationary satellites: a feasibility study with SEVIRI in the Southern North Sea," *Opt. Express* **17**, 14029–14052 (2009).
8. M. Ondrusek, E. Stengel, C. S. Kinkade, R. L. Vogel, P. Keegstra, C. Hunter, and C. Kim, "The development of a new optical total suspended matter algorithm for the Chesapeake Bay," *Remote Sens. Environ.* **119**, 243–254 (2012).
9. E. R. Knaeps, K. G. Ruddick, D. Doxaran, A. I. Dogliotti, B. Nechad, D. Raymaekers, and S. Sterckx, "A SWIR based algorithm to retrieve total suspended matter in extremely turbid waters," *Remote Sens. Environ.* **168**, 66–79 (2015).
10. Z. Mao, J. Chen, D. Pan, B. Tao, and Q. Zhu, "A regional remote sensing algorithm for total suspended matter in the East China Sea," *Remote Sens. Environ.* **124**, 819–831 (2012).
11. D. Doxaran, N. Cherukuru, and S. J. Lavender, "Apparent and inherent optical properties of turbid estuarine waters: measurements, empirical quantification relationships, and modeling," *Appl. Opt.* **45**, 2310–2324 (2006).
12. F. Shen, W. Verhoef, Y. Zhou, M. S. Salama, and X. Liu, "Satellite estimates of wide-range suspended sediment concentrations in Changjiang (Yangtze) Estuary using MERIS data," *Estuaries Coasts* **33**, 1420–1429 (2010).
13. H. R. Gordon and M. Wang, "Retrieval of water-leaving radiance and aerosol optical thickness over oceans with SeaWiFS: a preliminary algorithm," *Appl. Opt.* **33**, 443–452 (1994).
14. C. D. Mobley, "Estimation of the remote-sensing reflectance from above-surface measurements," *Appl. Opt.* **38**, 7442–7455 (1999).
15. Z.-P. Lee, Y.-H. Ahn, C. Mobley, and R. Arnone, "Removal of surface-reflected light for the measurement of remote-sensing reflectance from an above-surface platform," *Opt. Express* **18**, 26313–26342 (2010).
16. R. W. Preisendorfer, *Hydrologic Optics Vol. 1: Introduction* (National Technical Information Service, 1976).
17. J. R. V. Zaneveld, "A theoretical derivation of the dependence of the remotely sensed reflectance of the ocean on the inherent optical properties," *J. Geophys. Res.* **100**, 13135–13142 (1995).
18. A. Morel and B. Gentili, "Diffuse reflectance of oceanic waters (2): bi-directional aspects," *Appl. Opt.* **32**, 6864–6879 (1993).



19. H. R. Gordon and A. Morel, *Remote Assessment of Ocean Color for Interpretation of Satellite Visible Imagery: A Review* (Springer-Verlag, 1983), p. 44.
20. E. Knaeps, A. I. Dogliotti, D. Raymaekers, K. Ruddick, and S. Sterckx, "In situ evidence of non-zero reflectance in the OLCI 1020 nm band for a turbid estuary," *Remote Sens. Environ.* **120**, 133–144 (2012).
21. W. Shi and M. Wang, "Ocean reflectance spectra at the red, near-infrared, and shortwave infrared from highly turbid waters: a study in the Bohai Sea, Yellow Sea, and East China Sea," *Limnol. Oceanogr.* **59**, 427–444 (2014).
22. M. Wang and W. Shi, "The NIR-SWIR combined atmospheric correction approach for MODIS ocean color data processing," *Opt. Express* **15**, 15722–15733 (2007).
23. J. L. Mueller, G. S. Fargion, and C. R. McClain, *Ocean Optics Protocols For Satellite Ocean Color Sensor Validation, Revision 4* (Goddard Space Flight Center, 2003).
24. R. W. Austin, "Inherent spectral radiance signatures of the ocean surface," in *Ocean Color Analysis*, S. W. Duntley, ed. (Scripps Institution of Oceanography, 1974), pp. 1–20.
25. K. L. Carder and R. G. Steward, "A remote-sensing reflectance model of a red tide dinoflagellate off West Florida," *Limnol. Oceanogr.* **30**, 286–298 (1985).
26. J. Chen, E. D'sa, T. Cui, and X. Zhang, "A semi-analytical total suspended sediment retrieval model in turbid coastal waters: a case study in Changjiang River Estuary," *Opt. Express* **21**, 13018–13030 (2013).
27. L. Kou, D. Labrie, and P. Chylek, "Refractive indices of water and ice in the 0.65- to 2.5- $\mu$ m spectral range," *Appl. Opt.* **32**, 3531–3540 (1993).
28. A. Morel, B. Gentili, H. Claustre, A. Babin, A. Bricaud, J. Ras, and F. Tieche, "Optical properties of the 'clearest' natural waters," *Limnol. Oceanogr.* **52**, 217–229 (2007).
29. D. Doxaran, J. M. Froidefond, and P. Castaing, "Remote-sensing reflectance of turbid sediment-dominated waters. Reduction of sediment type variations and changing illumination conditions effects by use of reflectance ratios," *Appl. Opt.* **42**, 2623–2634 (2003).
30. M. Babin and D. Stramski, "Variations in the mass-specific absorption coefficient of mineral particles suspended in water," *Limnol. Oceanogr.* **49**, 756–767 (2004).
31. D. A. Kiefer and J. B. Soohoo, "Spectral absorption by marine particles of coastal waters of Baja California," *Limnol. Oceanogr.* **27**, 492–499 (1982).
32. S. Tassan and G. M. Ferrari, "Variability of light absorption by aquatic particles in the near-infrared spectral region," *Appl. Opt.* **42**, 4802–4810 (2003).
33. M. Kishino, M. Takahashi, N. Okami, and S. Ichimura, "Estimation of the spectral absorption coefficients of phytoplankton in a thermally stratified sea," *Bull. Mar. Sci.* **37**, 634–642 (1985).
34. D. G. Bowers and C. E. Binding, "The optical properties of mineral suspended particles: a review and synthesis," *Estuarine Coastal Shelf Sci.* **67**, 219–230 (2006).
35. R. Rottgers, C. Dupouy, B. B. Taylor, A. Bracher, and S. B. Wozniak, "Mass-specific light absorption coefficients of natural aquatic particles in the near-infrared spectral region," *Limnol. Oceanogr.* **59**, 1449–1460 (2014).
36. R. Astoreca, D. Doxaran, K. Ruddick, V. Rousseau, and C. Lancelot, "Influence of suspended particle concentration, composition and size on the variability of inherent optical properties of the Southern North Sea," *Cont. Shelf Res.* **35**, 117–128 (2012).
37. C. D. Mobley and L. K. Sundman, *HydroLight 5.2 User's Guide* (Sequoia Scientific, 2013).
38. M. Babin, A. Morel, V. Fournier-Sicre, F. Fell, and D. Stramski, "Light scattering properties of marine particles in coastal and open ocean waters as related to particle mass concentration," *Limnol. Oceanogr.* **48**, 843–859 (2003).
39. G. R. Fournier and J. L. Forand, "Analytic phase function for ocean water," in *Ocean Optics XII* (1994), pp. 194–201.
40. M. S. Twardowski, E. Boss, J. B. Macdonald, W. S. Pegau, A. H. Barnard, and J. R. V. Zaneveld, "A model for estimating bulk refractive index from the optical backscattering ratio and the implications for understanding particle composition in case I and case II waters," *J. Geophys. Res.* **106**, 14129–14142 (2001).
41. M. Zhang, J. Tang, Q. Song, and Q. Dong, "Backscattering ratio variation and its implications for studying particle composition: a case study in Yellow and East China seas," *J. Geophys. Res.* **115**, C12014 (2010).
42. M. Babin, D. Stramski, G. M. Ferrari, H. Claustre, A. Bricaud, G. Obolensky, and N. Hoepffner, "Variations in the light absorption coefficients of phytoplankton, nonalgal particles, and dissolved organic matter in coastal waters around Europe," *J. Geophys. Res.* **108**, 1–20 (2003).
43. A. Bricaud, M. Babin, A. Morel, and H. Claustre, "Variability in the chlorophyll-specific absorption coefficients of natural phytoplankton: analysis and parameterization," *J. Geophys. Res.* **100**, 13321–13332 (1995).
44. Z. P. Lee, K. L. Carder, and R. Arnone, "Deriving inherent optical properties from water color: a multi-band quasi-analytical algorithm for optically deep waters," *Appl. Opt.* **41**, 5755–5772 (2002).
45. M. S. Salama and W. Verhoef, "Two-stream remote sensing model for water quality mapping: 2SeaColor," *Remote Sens. Environ.* **157**, 111–122 (2015).
46. H. R. Gordon, O. B. Brown, and M. M. Jacobs, "Computed relationship between the inherent and apparent optical properties of a flat homogeneous ocean," *Appl. Opt.* **14**, 417–427 (1975).
47. A. Morel and B. Gentili, "Diffuse reflectance of oceanic waters: its dependence on sun angle as influenced by the molecular scattering contribution," *Appl. Opt.* **30**, 4427–4438 (1991).
48. A. Morel and B. Gentili, "Diffuse reflectance of oceanic waters, III, Implications of bi-directionality for the remote sensing problem," *Appl. Opt.* **35**, 4850–4862 (1996).
49. H. Loisel and A. Morel, "Non-isotropy of the upward radiance field in typical coastal (Case 2) waters," *Int. J. Remote Sens.* **22**, 275–295 (2001).
50. A. Morel, D. Antoine, and B. Gentili, "Bidirectional reflectance of oceanic waters: accounting for Raman emission and varying particle scattering phase function," *Appl. Opt.* **41**, 6289–6306 (2002).
51. J. T. O. Kirk, "A Monte Carlo study of the nature of the underwater light field in, and the relationships between optical properties of, turbid yellow waters," *Aust. J. Mar. Freshwater Res.* **32**, 517–532 (1981).
52. W. E. Vargas and G. A. Niklasson, "Applicability conditions of the Kubelka-Munk theory," *Appl. Opt.* **36**, 5580–5586 (1997).
53. C. Sandoval and A. D. Kim, "Deriving Kubelka-Munk theory from radiative transport," *J. Opt. Soc. Am. A* **31**, 628–636 (2014).
54. G. Zibordi and J.-F. Berthon, "Relationships between Q-factor and seawater optical properties in a coastal region," *Limnol. Oceanogr.* **46**, 1130–1140 (2001).
55. H. R. Gordon, O. B. Brown, R. H. Evans, J. W. Brown, R. C. Smith, K. S. Baker, and D. K. Clark, "A semianalytic radiance model of ocean color," *J. Geophys. Res.* **93**, 10909–10924 (1988).
56. A. Albert and C. D. Mobley, "An analytical model for subsurface irradiance and remote sensing reflectance in deep and shallow case-2 waters," *Opt. Express* **11**, 2873–2890 (2003).
57. Y.-J. Park and K. Ruddick, "Model of remote-sensing reflectance including bidirectional effects for case 1 and case 2 waters," *Appl. Opt.* **44**, 1236–1249 (2005).
58. C. D. Mobley, L. K. Sundman, and E. Boss, "Phase function effects on oceanic light fields," *Appl. Opt.* **41**, 1035–1050 (2002).
59. A. Morel and H. Loisel, "Apparent optical properties of oceanic water: dependence on the molecular scattering contribution," *Appl. Opt.* **37**, 4765–4776 (1998).
60. Z. P. Lee, K. L. Carder, and K. P. Du, "Effects of molecular and particle scatterings on model parameters for remote-sensing reflectance," *Appl. Opt.* **43**, 4957–4964 (2004).
61. T. J. Petzold, *Volume Scattering Functions for Selected Natural Waters* (Scripps Institution of Oceanography, 1972).
62. C. D. Mobley, *Light and Water: Radiative Transfer in Natural Waters* (Academic, 1994), p. 592.
63. R. Pope and E. Fry, "Absorption spectrum (380–700 nm) of pure waters: II. Integrating cavity measurements," *Appl. Opt.* **36**, 8710–8723 (1997).

64. E. S. Fry, "Visible and near-ultraviolet absorption spectrum of liquid water: comment," *Appl. Opt.* **39**, 2743–2744 (2000).
65. Z. Lee, J. Wei, K. Voss, M. Lewis, A. Bricaud, and Y. Huot, "Hyperspectral absorption coefficient of pure seawater in the range of 350–550 nm inverted from remote sensing reflectance," *Appl. Opt.* **54**, 546–558 (2015).
66. G. M. Hale and M. R. Querry, "Optical constants of water in the 200 nm to 200  $\mu$ m wavelength region," *Appl. Opt.* **12**, 555–563 (1973).
67. D. J. Segelstein, *The Complex Refractive Index of Water* (University of Missouri, 1981).
68. C. S. Roesler, M. J. Perry, and K. L. Carder, "Modeling *in situ* phytoplankton absorption from total absorption spectra in productive inland marine waters," *Limnol. Oceanogr.* **34**, 1510–1523 (1989).
69. IOCCG, Remote sensing of ocean colour in coastal, and other optically-complex, waters, in *Reports of the International Ocean-Colour Coordinating Group*, No. 3, S. Sathyendranath, ed. (IOCCG, 2000).
70. IOCCG, Remote sensing of inherent optical properties: fundamentals, tests of algorithms, and applications, in *Reports of the International Ocean-Colour Coordinating Group*, No. 5, Z.-P. Lee, ed. (IOCCG, 2006), p. 126.
71. M. L. Estapa, E. Boss, L. M. Mayer, and C. S. Roesler, "Role of iron and organic carbon in mass-specific light absorption by particulate matter from Louisiana coastal waters," *Limnol. Oceanogr.* **57**, 97–112 (2012).
72. A. Bricaud, A. Morel, and L. Prieur, "Absorption by dissolved organic matter of the sea (yellow substance) in the UV and visible domains," *Limnol. Oceanogr.* **26**, 43–53 (1981).
73. R. Doerffer and J. Fisher, "Concentrations of chlorophyll, suspended matter, and gelbstoff in case II waters derived from satellite coastal zone color scanner data with inverse modeling methods," *J. Geophys. Res.* **99**, 7457–7466 (1994).
74. S. Maritorena, D. A. Siegel, and A. R. Peterson, "Optimization of a semianalytical ocean color model for global-scale applications," *Appl. Opt.* **41**, 2705–2714 (2002).
75. D. Fylstra, L. Lasdon, J. Watson, and A. Waren, "Design and use of the Microsoft Excel Solver," *Interfaces* **28**, 29–55 (1998).
76. D. Doxaran, R. C. N. Cherukuru, and S. J. Lavender, "Estimation of surface reflection effects on upwelling radiance field measurements in turbid waters," *J. Opt. A* **6**, 690–697 (2004).
77. G. Zibordi, J.-F. Berthon, F. Mélin, D. D'Alimonte, and S. Kaitala, "Validation of satellite ocean color primary products at optically complex coastal sites: Northern Adriatic Sea, Northern Baltic Proper and Gulf of Finland," *Remote Sens. Environ.* **113**, 2574–2591 (2009).
78. Z.-P. Lee, N. Pahlevan, Y.-H. Ahn, S. Greb, and D. O'Donnell, "A robust approach to directly measure water-leaving radiance in the field," *Appl. Opt.* **52**, 1693–1701 (2013).
79. J. W. Campbell and W. E. Esaias, "Basis for spectral curvature algorithms in remote sensing of chlorophyll," *Appl. Opt.* **22**, 1084–1093 (1983).
80. F. Shen, Y.-X. Zhou, D.-J. Li, W.-J. Zhu, and M. S. Salama, "Medium resolution imaging spectrometer (MERIS) estimation of chlorophyll-a concentration in the turbid sediment-laden waters of the Changjiang (Yangtze) Estuary," *Int. J. Remote Sens.* **31**, 4635–4650 (2010).
81. A. A. Gitelson, J. F. Schalles, and C. M. Hladik, "Remote chlorophyll-a retrieval in turbid, productive estuaries: Chesapeake Bay case study," *Remote Sens. Environ.* **109**, 464–472 (2007).
82. G. Dall'Olmo, A. A. Gitelson, and D. C. Rundquist, "Towards a unified approach for remote estimation of chlorophyll-a in both terrestrial vegetation and turbid productive waters," *Geophys. Res. Lett.* **30**, 1938 (2003).
83. R. P. Stumpf, "Remote sensing of water clarity and suspended sediments in coastal waters," in *Proceedings of the First Thematic Conference on Remote Sensing for Marine and Coastal Environments*, New Orleans, LA, 1992.
84. K. Ruddick, B. Nechad, G. Neukermans, Y. Park, D. Doxaran, D. Sirjacobs, and J.-M. Beckers, "Remote sensing of suspended particulate matter in turbid waters: state of the art and future perspectives," in *Ocean Optics XIX*, Barga, Italy, 2008, 6–10.